

Switching in Cerebellar Stellate Cell Excitability in Response to a Pair of Inhibitory/Excitatory Presynaptic Inputs: A Dynamical System Perspective

Saeed Farjami

saeed.farjami@mcgill.ca

Department of Physiology, McGill University, Montreal, QC Canada H3G 1Y6

Ryan P. D. Alexander

ryan.alexander@mail.mcgill.ca

Derek Bowie

derek.bowie@mcgill.ca

Department of Pharmacology and Therapeutics, McGill University, Montreal, QC Canada H3G 1Y6

Anmar Khadra

anmar.khadra@mcgill.ca

Department of Physiology, McGill University, Montreal, QC Canada H3G 1Y6

Cerebellar stellate cells form inhibitory synapses with Purkinje cells, the sole output of the cerebellum. Upon stimulation by a pair of varying inhibitory and fixed excitatory presynaptic inputs, these cells do not respond to excitation (i.e., do not generate an action potential) when the magnitude of the inhibition is within a given range, but they do respond outside this range. We previously used a revised Hodgkin–Huxley type of model to study the nonmonotonic first-spike latency of these cells and their temporal increase in excitability in whole cell configuration (termed run-up). Here, we recompute these latency profiles using the same model by adapting an efficient computational technique, the two-point boundary value problem, that is combined with the continuation method. We then extend the study to investigate how switching in responsiveness, upon stimulation with presynaptic inputs, manifests itself in the context of run-up. A three-dimensional reduced model is initially derived from the original six-dimensional model and then analyzed to demonstrate that both models exhibit type 1 excitability possessing a saddle-node on an invariant cycle (SNIC) bifurcation when varying the amplitude of I_{app} . Using slow-fast analysis, we show that the original model possesses three equilibria lying at the intersection of the critical manifold of the fast subsystem and the nullcline of the slow variable h_A (the inactivation of the A-type K^+ channel), the middle equilibrium is of saddle type with two-dimensional stable manifold (computed from the reduced model) acting

as a boundary between the responsive and non-responsive regimes, and the (ghost of) SNIC is formed when the h_A -nullcline is (nearly) tangential to the critical manifold. We also show that the slow dynamics associated with (the ghost of) the SNIC and the lower stable branch of the critical manifold are responsible for generating the nonmonotonic first-spike latency. These results thus provide important insight into the complex dynamics of stellate cells.

1 Introduction

The cerebellum, in coordination with the brain, plays a central role in controlling body posture, movements, and some rhythmic physiological processes such as heart beats and breathing (Arshavsky & Orlovsky, 1986; Brooks & Thach, 2011; Holmes, 2000; Wolf, Rapoport, & Schweizer, 2009). The main electrical activities seen in the cerebellum are formed in the cerebellar cortex, which consists of three layers: the molecular layer on the top, the Purkinje layer in the middle, and the granular layer at the bottom (Miall, 2013; Palay & Chan-Palay, 1974). The GABAergic signals sent deep into the nuclei by the Purkinje cells are controlled by the interactions between inhibitory inputs from interneurons, such as basket and stellate cells (Korn & Axelrad, 1980), and excitatory inputs from parallel and climbing fibers (Eccles, Llinás, & Sasaki, 1964; Morton & Bastian, 2004). Cerebellar stellate cells also receive excitatory and inhibitory inputs from parallel fibers and other stellate cells (Albus, 1971; Liu, Lachamp, Liu, Savtchouk, & Sun, 2011), making such presynaptic inputs play a significant role in determining the type of activities generated by Purkinje cells (Midtgaard, 1992b; Mittmann, Koch, & Häusser, 2005).

Stellate cells are spontaneously active; they tonically fire action potentials (APs) when isolated (Häusser & Clark, 1997; Llano & Marty, 1995; Midtgaard, 1992a). However, recent experimental evidence suggests that the intrinsic excitability properties of these neurons (including firing threshold, firing frequency, and first-spike latency) temporally change during whole-cell configuration before they all eventually stabilize around 30 min post-sealing/breakthrough into the cell (Molineux, Fernandez, Mehaffey, & Turner, 2005). This phenomenon was previously termed run-up and was investigated dynamically using a revised Hodgkin–Huxley (HH) type model (Mitry, Alexander, Farjami, Bowie, & Khadra, 2020) that was adopted from (Anderson et al., 2010; Molineux et al., 2005). The model consists of five ionic currents: fast Na^+ (I_{Na}), delayed rectifier K^+ (I_{K}), A-type K^+ (I_{A}), T-type Ca^{2+} (I_{T}), and leak (I_{L}) currents. The study in Alexander, Mitry, Sareen, Khadra, and Bowie (2019) showed that the increase in excitability during run-up from 0 min (pre-run-up) to 30 min (post-run-up) is due to shifts in the activation and inactivation curves of I_{Na} and I_{A} . This model was shown to exhibit type 1 excitability and to possess a saddle-node on an

invariant cycle (SNIC) bifurcation, a hallmark of type I excitability (Franci, Drion, & Sepulchre, 2012; Izhikevich, 2000), when the membrane potential was plotted as a function of applied current I_{app} . During run-up, the SNIC was shown to shift both downward, indicating a more hyperpolarized firing threshold, and leftward, indicating a lower rheobase (Mitry et al., 2020). The ghost of the SNIC (Izhikevich, 2006; Sherman & Ha, 2017) was also shown to produce a slow region in state-space through which solution trajectories travel at a slower rate, producing intriguing dynamics.

One peculiar feature of stellate cells is their ability to generate non-monotonic first-spike latency as a function of membrane holding potential (Molineux et al., 2005). More specifically, when these neurons are presented with decreasing magnitudes of hyperpolarizing holding potential (bias current I_{bias}), followed by a fixed depolarizing test current (I_{test}) in a step protocol, their first-spike latency initially increases, then decreases until it reaches a plateau. It was shown that the nonmonotonic latency profile is caused by the differences in $V_{1/2}$ of the steady-state inactivation parameters of the outward A-type K^+ and low-threshold inward T-type Ca^{+2} channels (Molineux et al., 2005). Further analysis of this feature (Mitry et al., 2020) revealed that the nonmonotonic latency is preserved during run-up. Moreover, the latency can be made arbitrarily large if the amplitude of I_{test} in the step current is chosen in such a way that the response of the system lies very close to the stable invariant manifold of a saddle or a saddle-node equilibrium (Mitry et al., 2020). Mitry et al. (2020) have suggested that the ghost of the SNIC, along with the “distance” from an attracting periodic orbit (starting from a given holding potential), are both involved in producing the nonmonotonic latency profile. The effects of these two factors individually or collectively on the response of the system, however, have not been tackled.

Stellate cells also show interesting dynamics in response to a pair of inhibitory and excitatory presynaptic (dynamic) inputs. Indeed, experimental evidence has shown that applying three pairs of such presynaptic inputs with increasing magnitude of inhibition (starting from 0 pS), while keeping the magnitude of excitation fixed, causes the cell to switch from being responsive (able to fire an action potential, AP) to nonresponsive (unable to fire an AP) and back to responsive again (Molineux et al., 2005). This means that the middle pair of presynaptic inputs with an intermediate magnitude of inhibition produces “paradoxically” a graded response (without an AP). Prior to firing an AP, however, the response generated by the third pair (when the inhibition is high) is actually slightly lower in amplitude than the one generated by the middle pair, indicating that the AP firing threshold is not well characterized. In other words, the firing threshold is modified when the amplitude of the inhibition is varied. The revised HH-type model in Mitry et al. (2020) was successful in capturing both of these phenomena during pre- and post-run-up, namely, the nonmonotonic latency profile and the switching in responsiveness. For the latter, it was shown that the model

can switch three times (rather than once) between responsive and nonresponsive regimes as the magnitude of the inhibition is monotonically increased without explaining how the switching phenomenon is dynamically produced.

In this study, we analyze the response of stellate cells to such inhibitory and excitatory presynaptic inputs, using a dynamical systems approach, to decipher their various activities. Applying a slow-fast analysis, we explain how the ghost of the SNIC, along with the traveling time from a steady state to an attracting periodic orbit, plays roles in generating the switching phenomenon and the nonmonotonic first-spike latency. We do so using the revised pre- and post-run-up HH-type model introduced in Molineux et al. (2005) and then reparameterized in Mitry et al. (2020). The bifurcation analysis performed in Mitry et al. (2020) is expanded in new directions by adapting advanced and efficient computational techniques, such as the two-point boundary value problem (2PBVP) and continuation in Auto, to recompute the nonmonotonic first-spike latency and the boundary defining the switching in responsiveness (all of which were previously computed manually). Because of the computational efficiency of these techniques, we explore a larger parameter space and provide an explanation as to how the slow region formed by the ghost of the SNIC is created and how it can give rise to nonmonotonic latency. Model reduction is then applied to show that at least three dimensions are needed to generate the switching phenomenon, and a comparison between the full and reduced models is conducted to demonstrate that they are both type 1 oscillators possessing a SNIC bifurcation with respect to the applied current I_{app} . In our slow-fast analysis, we treat the inactivation of A-type K^+ as the slow variable. We conclude, based on this analysis, that (the ghost of) the SNIC is formed when the h_A -nullcline is (nearly) tangential to the critical manifold of the fast subsystem. Furthermore, we show that the slow dynamics caused by the ghost of the SNIC is due to the bottleneck effect created when the h_A -nullcline and the critical manifold of the fast subsystem are close (Rinzel & Baer, 1988; Sardanyés, 2009). Our analysis also reveals that this slow dynamics, together with how long trajectories travel along the lower branch of the critical manifold, produces the nonmonotonic first-spike latency profile.

2 Methods

2.1 Mathematical Model. A revised HH-type model for cerebellar stellate cell electrical excitability was previously developed (Mitry et al., 2020). The model more accurately captures the experimental data during both pre- and post-run-up with a few changes in parameter values of the steady-state (in)activation curves of ionic currents from the original model presented in Molineux et al. (2005).

The revised five-dimensional model, referred to hereafter as the full system, is given by

$$\begin{cases} C\dot{V} = I_{\text{app}} - I_{\text{Na}} - I_{\text{K}} - I_{\text{L}} - I_{\text{A}} - I_{\text{T}} \\ \dot{x} = (x_{\infty} - x)/\tau_x, \quad x = h, n, n_{\text{A}}, h_{\text{A}}, h_{\text{T}}, \end{cases} \quad (2.1)$$

where C is the membrane capacitance, I_{app} is the applied current, x is the gating variable of each ionic current I_{η} ($\eta = \text{Na}, \text{K}, \text{L}, \text{A}, \text{T}$), x_{∞} is its steady state, and τ_x is its time constant. The ionic currents are

$$\begin{aligned} I_{\text{Na}} &= g_{\text{Na}} m_{\infty}^3 h (V - E_{\text{Na}}), \\ I_{\text{K}} &= g_{\text{K}} n^4 (V - E_{\text{K}}), \\ I_{\text{L}} &= g_{\text{L}} (V - E_{\text{L}}), \\ I_{\text{A}} &= g_{\text{A}} n_{\text{A}} h_{\text{A}} (V - E_{\text{K}}), \\ I_{\text{T}} &= g_{\text{T}} m_{\text{T},\infty} h_{\text{T}} (V - E_{\text{Ca}}), \end{aligned}$$

where g_{η} is the maximum ionic conductance, E_{η} is the reversal potential, m_{∞} is the steady-state activation of I_{Na} , and $m_{\text{T},\infty}$ is the steady-state activation of I_{T} . These functions and parameters are the same as those presented by Mitry et al. (2020). The steady-state (in)activation functions are of the form

$$x_{\infty} = \frac{1}{e^{-(V-v_x)/s_x}}, \quad x = m, h, n, n_{\text{A}}, h_{\text{A}}, m_{\text{T}}, h_{\text{T}}.$$

The time constant for the inactivation of Na^+ current is given by

$$\tau_h = y_0 + \frac{2Aw}{4\pi(V - V_c)^2 + w^2},$$

and the time constant for the activation of K^+ current is given by

$$\tau_n = \frac{6}{1 + e^{(V+23)/15}}.$$

Parameter values of the full system (during both pre- and post-run-up) are identical to those presented in Mitry et al. (2020) and are listed in Tables 1 and 2.

To study the response of the system to stimulation, we use either a current-step protocol $I_{\text{app}} = I_{\text{bias}} + (I_{\text{test}} - I_{\text{bias}})\mathcal{H}(t - t^*)$, where $\mathcal{H}(t - t^*)$ is the Heaviside step function, consisting of a bias current (I_{bias}) that hyperpolarizes the stellate cell model to a rest state (holding membrane potential), followed by a test current (I_{test}) applied at $t = t^*$ that depolarizes the stellate cell model above the threshold, or apply a presynaptic (dynamic) input $I_{\text{app}} = I_{\text{bias}} + (I_{\text{syn}} - I_{\text{bias}})\mathcal{H}(t - t^*)$ (Mitry et al., 2020; Molineux et al., 2005), where I_{syn} is the sum of two alpha functions, one of which is shifted 15 time

Table 1: Parameter Values of the Full System, Equation 2.1, and the Reduced Model, Equation 2.3, That Do Not Change During Run-Up.

Parameter	Value	Parameter	Value	Parameter	Value
C	1.50148 $\mu\text{F}/\text{cm}^2$	g_{Na}	3.4 mS/cm^2	E_{Na}	+55 mV
A	322 ms.mV	g_{K}	9.0556 mS/cm^2	E_{K}	-80 mV
y_0	0.1 ms	g_{L}	0.07407 mS/cm^2	E_{L}	-38 mV
V_c	-74 mV	g_{A}	15.0159 mS/cm^2	E_{K}	-80 mV
w	46 mV	g_{T}	0.45045 mS/cm^2	E_{Ca}	+22 mV

Table 2: Parameter Values of the (In)activation Functions of the Full System, Equation 2.1, and the Reduced Model, Equation 2.3.

Current	Activation			Inactivation		
	v_x (mV)	s_x (mV)	τ_x (ms)	v_x (mV)	s_x (mV)	τ_x (ms)
I_{Na}	-37 (-44)	3.0	-	-40 (-48.5)	-4.0	$\tau_h(V)$
I_{K}	-23	5.0	$\tau_h(V)$	-	-	-
I_{A}	-27 (-41)	13.2	5	-80 (-96)	-6.5 (-9.2)	10
I_{T}	-50	3.0	-	-68	-3.75	15

Note: Two values are presented for parameters that are affected by run-up (without parentheses: pre-run-up; between parentheses: post-run-up).

units away from the origin, given by

$$I_{\text{syn}} = g_{\text{inh}} t (V + 82) e^{-\alpha_1 t} \mathcal{H}(t) + g_{\text{exc}} (t - 15) V e^{-\alpha_2 (t-15)} \mathcal{H}(t - 15). \quad (2.2)$$

Figure 2A shows a graphical illustration of such a presynaptic input. The magnitude of the inhibition/excitation ($g_{\text{inh}}/g_{\text{exc}}$) will be varied throughout this study, whereas $\alpha_1 = -1.25 \text{ ms}^{-1}$ and $\alpha_2 = -3 \text{ ms}^{-1}$ are kept fixed.

Like all other HH-type models, differences in timescales between the different variables of the full system, equation 2.1, exist. A straightforward way to assess the timescale separation of these variables is to compare the maximum changes occurring in their derivatives over a full AP cycle. This is done in Figure 1, where the time traces of the derivatives of the gating variables— \dot{h} (black), \dot{n} (green), \dot{n}_{A} (orange), \dot{h}_{A} (blue), and \dot{h}_{T} (red)—of system 2.1 are shown, indicating that h_{A} is the slowest variable and can be treated as a parameter in our slow-fast analysis. According to Figure 1, the gating variable h_{T} is also slow and can be treated as a parameter, but it is not as slow as h_{A} .

2.2 Model Reduction. There are always limitations to visualizing topological objects with more than three dimensions, produced by

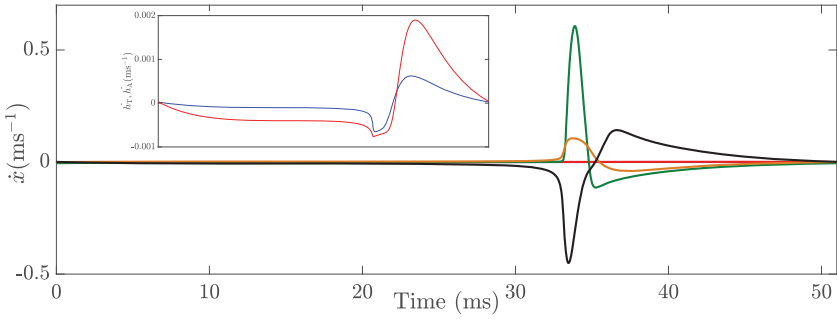


Figure 1: Time traces of variations in the (in)activation variables of ionic currents— \dot{h} (black), \dot{i} (green), \dot{i}_A (orange), \dot{h}_A (blue), and \dot{h}_T (red)—during a full AP cycle. The curves \dot{h}_A and \dot{h}_T are very close to one another and are not discernible. The inset shows a magnification of these two curves.

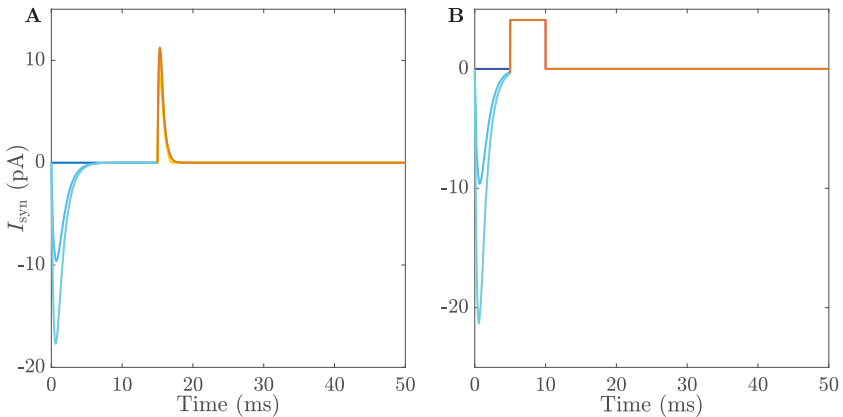


Figure 2: (A) Graphical representation of the presynaptic input defined by equation 2.2, whose inhibitory (different shades of blue) and excitatory (different shades of orange) components are both dynamic. (B) Graphical representation of the presynaptic input defined by equation 2.4, whose inhibitory component (different shades of blue) is dynamic but excitatory component (orange) is a current pulse.

high-dimensional systems. With a five-dimensional model like the full system, equation 2.1, it is not possible to visualize the geometry of topological objects such as manifolds associated with saddle-type steady states and limit cycles.

To resolve this problem, we develop a reduced model analogous to system 2.1. This is done by replacing the inactivation of Na^+ current h by $1 - n$,

where n is the activation variable of K^+ current, as well as replacing the activation and inactivation variables of A-type K^+ current, n_A and h_A , by n and h_T , respectively, where h_T is the inactivation of T-type Ca^{2+} channel. This generates a new current, given by $I_X := g_K n h_T (V - V_K)$. The resulting three-dimensional model (referred to hereafter as the reduced model) becomes

$$\begin{cases} C\dot{V} = I_{app} - g_{Na} m_{\infty}^3 (1 - n)(V - V_{Na}) - g_K n^4 (V - V_K) \\ \quad - g_L (V - V_L) - g_K n h_T (V - V_K) - g_T m_{T,\infty} h_T (V - V_{Ca}) \\ \dot{n} = (n_{\infty} - n)/\tau_n \\ \dot{h}_T = (h_{T,\infty} - h_T)/15, \end{cases} \quad (2.3)$$

where the steady-state (in)activation functions m_{∞} , n_{∞} , $m_{T,\infty}$ and $h_{T,\infty}$ are the same as those presented for system 2.1 and specified in section 2.1. Its parameter values are provided in Tables 1 and 2. The reduced model differs from the full system in many respects, but as we will see, it preserves some of the dynamics of the full system and can be used to provide insight into how switching in responsiveness is produced. It is important to point out here that applying such a model reduction by substituting the (in)activation functions of certain voltage-gated ion channels with other equivalent ones has been previously used to simplify the analysis (Börger, 2017; Fernandez, Engbers, & Turner, 2007; Krinskii & Kokoz, 1973). Indeed, by doing so, the computation and visualization of (un)stable manifolds of steady states and periodic orbits become feasible, shedding light on the nontrivial dynamics of the full system that are otherwise undecipherable.

2.3 Simplification of the Presynaptic Input. We expect that the structure of the full system becomes displaced or deformed during the application of the excitatory component of the presynaptic input defined by equation 2.2. This will be problematic when studying how this structure governs switching in responsiveness, one of the key features we are analyzing. To resolve this issue, we replace the excitatory component of the alpha function in equation 2.2 by a current square pulse applied for 5 ms while the dynamic inhibitory input (applied for 5 ms) is removed as soon as the excitatory input is applied. The application of such excitatory input will not displace or deform the bifurcation structure of the full system and keep it frozen in time during the application of excitatory pulse and when there is no more input (i.e., after removing the pulse). With these simplifications, we obtain the following expression for the presynaptic input,

$$I_{syn} = g_{inh} t (V + 82) e^{-\alpha_1 t} \mathcal{H}(t) \mathcal{H}(5 - t) + g_{exc} \mathcal{H}(t - 5) \mathcal{H}(10 - t), \quad (2.4)$$

where α_1 is the same as in equation 2.2. For a graphical illustration of such presynaptic input, see Figure 2B.

2.4 Software and Numerical Methods. We use the pseudo-arc-length continuation software package Auto (Doedel, 1981; Doedel & Oldeman, 2010) for computing the bifurcation diagrams and the latency profiles throughout the letter with the help of XPPAUT (freeware developed by Bard Ermentrout available online at <http://www.math.pitt.edu/~bard/xpp/xpp.html>). The code for regenerating the figures is available online (Farjami, Alexander, Bowie, & Khadra, 2019).

We also adapt a 2PBVP technique to compute the stable manifold of a saddle equilibrium of the reduced model as a family of orbit segments in Auto. Here, we briefly explain how we use 2PBVP to do so (for a detailed description, see Krauskopf et al., 2005). Each orbit segment $u(s) \in \mathbb{R}^3$ ($0 \leq s \leq 1$), which lies on the manifold, is a solution of the rescaled system,

$$\dot{u} = TF(u), \quad (2.5)$$

where F is the right-hand side of the reduced model, equation 2.3.

A set of three boundary conditions is also needed to make the orbit segment a well-defined solution of the rescaled system, equation 2.5. These boundary conditions can be arbitrarily distributed at the start (k) and at the end ($3 - k$) of each orbit segment, where $k = 1, 2, \text{ or } 3$. The boundary conditions are (hyper)surfaces transverse to the start and end of each orbit segment. For example, suppose we have a system that possesses a saddle equilibrium with two negative eigenvalues. To compute the two-dimensional stable manifold of the equilibrium, we choose $k = 2$ boundary conditions at the start of the orbit segment. These boundary conditions lie along the circumference of a tiny ellipse around the equilibrium in the plane spanned by the stable eigenvectors corresponding to the negative eigenvalues of the saddle equilibrium. There are many ways to choose the other $3 - k = 1$ boundary condition at the end of the orbit segments; for instance, it can be set to a plane, a sphere, or any surface transverse to the orbit segments, to name just a few. Changing one of the boundary conditions along the ellipse circumference generates a family of orbit segments that together form the manifold. Note that the first orbit of the manifold can be computed by integrating backward in time or using a homotopy step (Krauskopf et al., 2005; Farjami, Kirk, & Osinga, 2018). This is the technique used for computing the two-dimensional stable manifold of the saddle equilibrium that belongs to the reduced model, equation 2.3.

We also use 2PBVP to recompute the latency profile in a more computationally efficient and systematic manner than previously done in Mitry et al. (2020). The same as for computing the stable manifold, we first rescale the orbit segments to the time interval $[0,1]$. We then set three boundary conditions at the start of the first orbit segment in such a way that the start of each orbit segment lies at a stable equilibrium of the full system when it is hyperpolarized by I_{bias} and no I_{test} is applied. We also set the boundary conditions

at the end of the orbit segments on top of the first spike with respect to the membrane potential when $dV/dt = 0$. The first response of the full system is computed for a fixed value of I_{bias} by integrating forward in time while I_{test} is applied. The computation is stopped as soon as $dV/dt = 0$ is satisfied. Varying I_{bias} in the current-step protocol while keeping the integration time free and $dV/dt = 0$ at the end of each orbit segment generates the nonmonotonic profile of the first-spike latency. Note that we use the same value of I_{test} for computing each nonmonotonic first-spike latency profile.

When the full system is not responsive to dynamic presynaptic inputs, the first-spike latency of the response is infinite. To compute the boundary between responsive and nonresponsive regimes, we use a similar 2PBVP setup and let the magnitude of inhibition g_{inh} (or excitation g_{exc}) vary. The latency increases unboundedly as g_{inh} (g_{exc}) approaches the boundary due to a connection from a stable to a saddle equilibrium. We set the latency at a very large value and approximate the boundary in the $(g_{\text{exc}}, g_{\text{inh}})$ -plane. One can use Lin's method (Krauskopf & Riess, 2008) to detect the moment of connection between the stable and saddle equilibria and continue the boundary in $(g_{\text{exc}}, g_{\text{inh}})$ -plane while the connection is preserved.

3 Results

3.1 Type I Excitability and Nonmonotonic Latency Profile. Mitry et al. (2020) showed that the bifurcation diagram of the full system, equation 2.1, with respect to I_{app} produces a saddle-node on an invariant cycle (SNIC) bifurcation, where a family of periodic orbits and a saddle-node bifurcation of equilibria meet and the firing period becomes infinitely large. Figure 3 shows that, indeed, the bifurcation diagrams of system 2.1 with respect to I_{app} for the pre- and post-run-up parameter sets exhibit the same underlying dynamics manifested as type 1 excitability, with three branches of stable (solid) and unstable or saddle (dotted) equilibria (black lines) merging at two saddle-node bifurcations, denoted F_1 and F_2 . The envelopes of limit cycles (green lines), representing the maxima and minima of the periodic orbits with respect to V , consist of stable (solid) and unstable (dotted) branches of limit cycles. The envelopes of stable limit cycles terminate at a SNIC bifurcation, while the envelopes of unstable limit cycles emanate from a subcritical Hopf bifurcation, denoted H. These envelopes of stable and unstable limit cycles eventually meet at a saddle-node bifurcation of periodic orbits, denoted FP.

The slow region associated with the ghost of the SNIC (the region created by values of I_{app} to the right of F_1 where the periodic branch is stable), along with the "location" of the initial condition (determined by a hyperpolarizing bias-current $I_{\text{app}} = I_{\text{bias}}$ preceding a depolarizing test current $I_{\text{app}} = I_{\text{test}}$ in the current-step protocol) relative to the attracting periodic orbit give rise to the nonmonotonic latency profiles (Mitry et al., 2020). Figure 4 shows that the model produces first-spike latency profiles that are

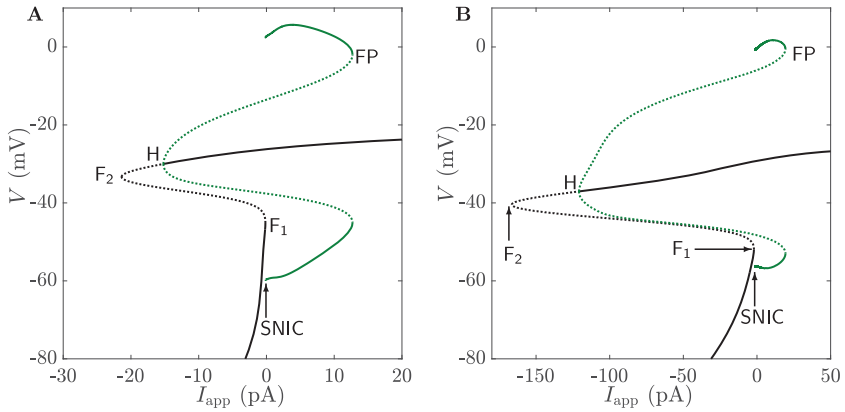


Figure 3: Bifurcation diagrams of the full system, equation 2.1, with respect to I_{app} during (A) pre- and (B) after-run-up. Black solid (dotted) lines indicate branches of stable (unstable/saddle) equilibria; green solid (dotted) lines show envelopes of stable (unstable) limit cycles. Two saddle-node bifurcations F_1 and F_2 connect three branches of equilibria. The envelopes of unstable limit cycles emanating from a subcritical Hopf bifurcation H collide with the envelopes of stable limit cycles at a saddle-node bifurcation of periodic orbits, FP . The envelopes of stable limit cycles eventually terminate at a $SNIC$ bifurcation.

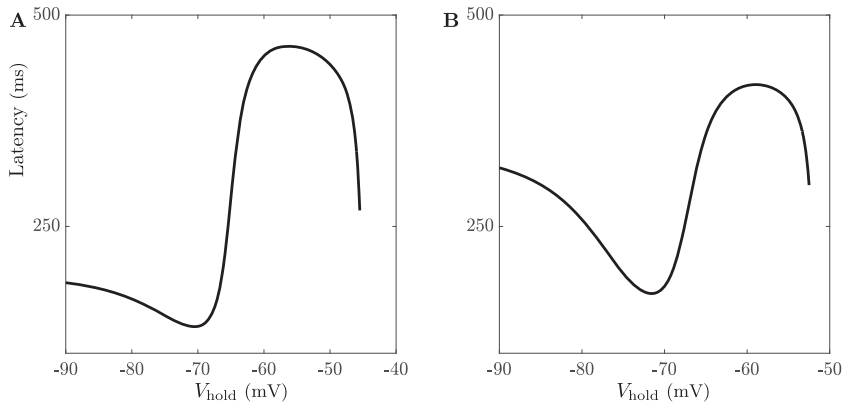


Figure 4: Nonmonotonic first-spike latency of the full system, equation 2.1, with respect to the holding potential V_{hold} for (A) pre-, and (B) post-run-up, computed using the 2PBVP and continuation methods. The difference between I_{test} and I_{SNIC} is almost the same for both cases. The applied test current I_{test} for pre- and post-run-up are -0.17 pA and -0.24 pA, respectively.

nonmonotonic, computed systematically and efficiently using 2PBVP, for the two sets of parameters corresponding to Figure 3A (before run-up) and Figure 3B (after run-up). Mitry et al. (2020) showed that these latency profiles (previously computed manually for each pulse) can be made arbitrarily large for a wider range of holding potentials during the post-run-up period (corresponding to the biphasic component and the tail of the profile, but not in between), while this is more limited during pre-run-up (restricted only to the nonmonotonic component of the profile) as $I_{\text{test}} \rightarrow I_{\text{SNIC}}^+$. As shown in Figure 3, when $I_{\text{app}} = I_{\text{SNIC}}$, there are two equilibria in the full system, equation 2.1. One of these equilibria is a saddle-node possessing a stable manifold. Therefore, perturbing the system from its resting state by applying $I_{\text{app}} = I_{\text{test}}$ while $I_{\text{test}} \rightarrow I_{\text{SNIC}}^+$ makes the response of the system lie directly on the stable manifold of the saddle-node and, as a result, causes the first-spike latency to become unbounded. It was further demonstrated that the remaining range of holding potentials associated with post-run-up can still produce transient single-spike activity when $I_{\text{app}} = I_{\text{test}} < I_{\text{SNIC}}^+$. In this latter case (see Figure 4), the full system, equation 2.1, has three equilibria, one of which (middle) is of a saddle type possessing a stable manifold (SMS). Applying a test current $I_{\text{app}} = I_{\text{test}} = I_{\text{SMS}}$, which makes the response of the system land exactly on the stable manifold of the saddle equilibrium, gives rise to infinite latency in the single transient spike regime (Mitry et al., 2020). Succinctly, the location of the initial conditions, as specified by the holding potential, relative to the stable manifolds of both the saddle-node or saddle, was shown to be the key determinant of such outcomes (Mitry et al., 2020).

3.2 Slow-Fast Analysis. In many physiological systems, some processes may evolve significantly faster than others. In neurons, membrane voltage, together with some gating variables (e.g., the Na^+ activation variable), is dynamically faster relative to the other variables such as Ca^{2+} (Ermentrout & Terman, 2010; Keener & Sneyd, 2009). One can thus apply timescale separation and slow-fast analysis to study the rich dynamics of such systems. That involves treating the slow variables as parameters and studying the dynamics of the fast subsystem in response to perturbations in these parameters. This can provide valuable insights into the dynamics of the full system (Desroches et al., 2012).

In this section, we apply these techniques and treat the slowest variable h_A of the full system, equation 2.1, as a parameter; the remaining part of the model will be called the fast subsystem. Note that h_T is also slow; treating it, however, as a parameter along with h_A produces bifurcation structures that are identical to those presented below (results not shown). A plot of the bifurcation diagram of the membrane voltage V (one of the variables of the fast subsystem) onto the (V, h_A) -plane is shown in Figure 5. The line of stable (solid) and unstable/saddle (dotted) equilibria of the fast subsystem (black line) has four branches separated by three saddle-node bifurcations, denoted SN_1 , SN_2 , and SN_3 . The equilibria on branches between SN_1 and

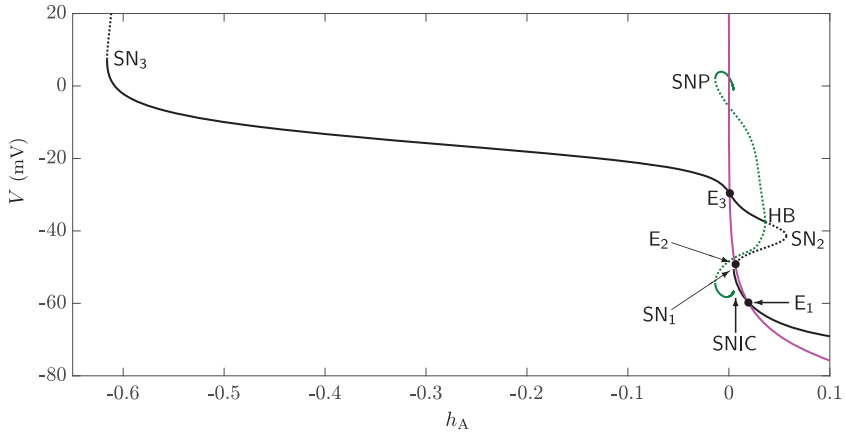


Figure 5: Bifurcation diagram of the fast subsystem of system 2.1 for the set of post-run-up parameters in (V, h_A) -plane and for $I_{\text{bias}} = -0.6$ pA. Black solid (dotted) lines indicate stable (unstable/saddle) branches of equilibria; green solid (dotted) lines correspond to envelopes of stable (unstable) limit cycles; the magenta line is the h_A -nullcline in the (V, h_A) -plane. Four branches of stable and unstable/saddle equilibria of the fast subsystem, separated by three saddle-node bifurcations SN_1 , SN_2 , and SN_3 , form the critical manifold of the full system. The envelope of unstable limit cycles (green) emanating from a subcritical Hopf bifurcation (HB) undergoes a saddle-node bifurcation of periodic orbits (SNP) and terminates at a SNIC bifurcation. The h_A -nullcline intersects the critical manifold at E_1 , E_2 , and E_3 , representing the equilibria of the full system, equation 2.1.

SN_2 and beyond SN_3 for large values of V are of the saddle type, whereas the equilibria on the other two branches, namely, between SN_2 and SN_3 and beyond SN_1 for large values of h_A , are stable. The equilibria between SN_2 and SN_3 become unstable at a subcritical Hopf bifurcation (HB). The maxima and minima of the family of periodic orbits with respect to V form envelopes of limit cycles (green). The envelope of unstable limit cycles (dotted) emanating from HB undergoes a saddle-node bifurcation of periodic orbits (SNP) with the envelope of stable limit cycles (solid). This latter envelope eventually terminates at a SNIC bifurcation.

Figure 5 also shows the h_A -nullcline (magenta), a hypersurface in a six-dimensional space, whose intersection with the (h_A, V) -plane is plotted. The nullcline intersects the critical manifold of the fast subsystem at three equilibria on different branches, denoted E_1 , E_2 , and E_3 . The equilibria E_1 and E_3 are attracting, while E_2 is of a saddle type. When a step current is applied, the critical manifold gets deformed slightly, but the h_A -nullcline remains unaltered, keeping the order and stability properties of these three

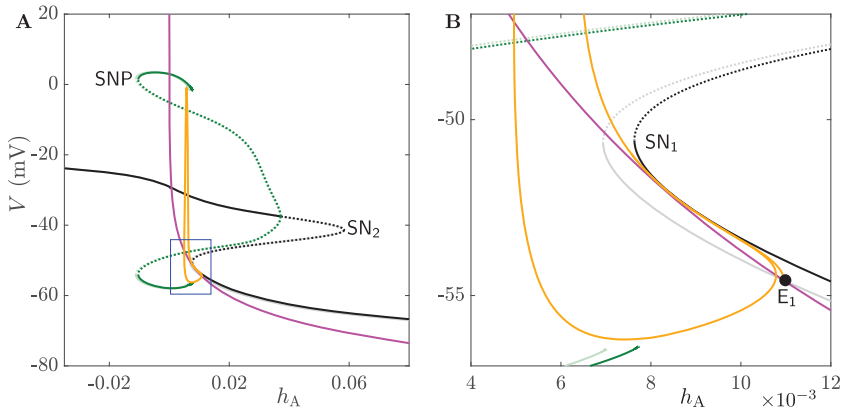


Figure 6: (A) The response (orange) of the full system, equation 2.1, during post-run-up for $I_{\text{test}} = -0.2$ pA starting from the equilibrium E_1 set by $I_{\text{bias}} = -0.3$ pA. The response is projected onto the two bifurcation diagrams of the membrane voltage V with respect to the inactivation variable h_A for $I_{\text{app}} = I_{\text{bias}}$ (faded colors) and $I_{\text{app}} = I_{\text{test}}$ (dark colors). The faded bifurcation diagram is not clearly visible because it is very close to the dark bifurcation diagram. The h_A -nullcline (magenta) is also plotted in the figure. (B) Magnification of the curves inside the blue box in panel A, highlighting dynamics near the left knees (SN_1) of the faded and dark bifurcation diagrams.

steady states unchanged. It should be noted that the direction of the flow of solution trajectories on the right (left) side of the h_A -nullcline is to the left (right).

To explain how the ghost of the SNIC in this system manifests itself, we focus here on the parameter range between the saddle-node bifurcation of periodic orbits (SNP) and the right saddle-node (SN_2). Figure 6 shows the projection of the solution trajectory of the full system, equation 2.1, (orange) during post-run-up generated by a current-step protocol with $I_{\text{bias}} = -0.3$ pA and $I_{\text{test}} = -0.2$ pA. The response is superimposed onto the bifurcation diagram of the fast subsystem, together with the h_A -nullcline shown in Figure 5. Because of the step current applied on the full system, one would expect the system to produce two bifurcation diagrams for V with respect to h_A at $I_{\text{bias}} = -0.3$ pA and at $I_{\text{test}} = -0.2$ pA. Plotting these two bifurcation diagrams in faded and dark colors, respectively, in Figure 6A reveals that they are almost overlaying on top of each other (with the former not discernible from the latter). Nonetheless, applying I_{test} still induces a slight rightward shift in the bifurcation diagram of the fast subsystem (see Figure 6B). This causes the intersection of the faded bifurcation diagram with the h_A -nullcline—the stable equilibrium E_1 representing the initial condition for the solution trajectory—to disappear. As a result, when applying

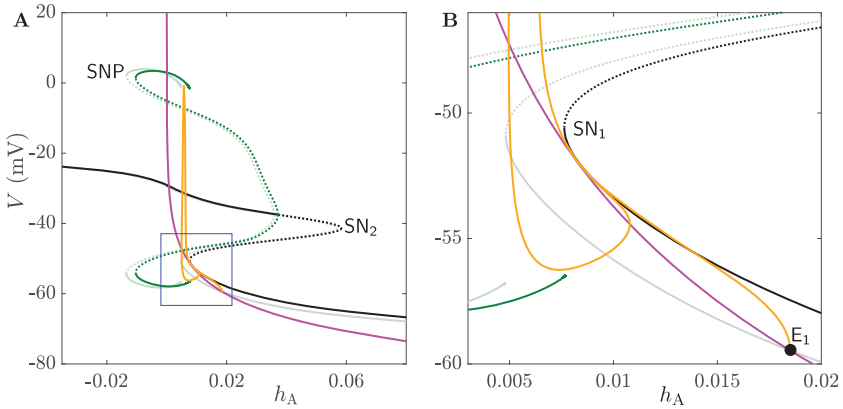


Figure 7: (A) The response (orange) of the full system, equation 2.1, during post-run-up for $I_{\text{test}} = -0.2$ pA starting from the equilibrium E_1 set by $I_{\text{bias}} = -0.6$ pA. The response is projected onto the two bifurcation diagrams of the membrane voltage V with respect to the inactivation variable h_A for $I_{\text{app}} = I_{\text{bias}}$ (faded colors) and $I_{\text{app}} = I_{\text{test}}$ (dark colors). The h_A -nullcline (magenta) is also plotted in the figure. (B) Magnification of the curves inside the blue box in panel A, highlighting dynamics near the left knees (SN_1) of the faded and dark bifurcation diagrams.

the step current, the trajectory moves toward the lower branch of the critical manifold and then jumps up toward the envelope of stable limit cycles where it starts oscillating. This limit cycle represents an attracting periodic orbit of the full system.

As shown in Figure 6B, the h_A -nullcline and the equilibrium branch of the fast subsystem are very close to each other near SN_1 when $I_{\text{app}} = I_{\text{test}} = -0.2$ pA. This means that the full system is about to undergo a saddle-node bifurcation. The created passage is called the “ghost of a bifurcation” or “slow region,” characterized by a very slow flow of trajectories and no well-defined boundary. In other words, \dot{x} is very close to zero for $x = V, h, n, n_A, h_A, h_T$ in this region. Prior to the application of I_{test} , when $I_{\text{bias}} = -0.3$ pA, E_1 is very close to SN_1 , thereby generating a trajectory for the full system that takes a short path through the slow region. The first-spike latency for such trajectories in this case is not large, even though they evolve very slowly through the slow region.

As already discussed, initially for high holding potentials, the latency of the response of the full system, equation 2.1, significantly increases when the bias current I_{bias} decreases (see Figure 4). For $I_{\text{bias}} = -0.6$ pA, the latency is large, and the slow-fast configuration in Figures 7A and 7B shows that E_1 moves toward a smaller V -value along the h_A -nullcline. This means that the

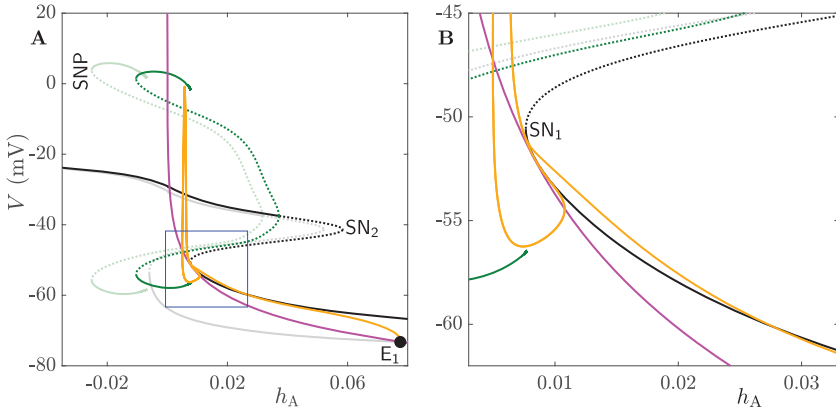


Figure 8: (A) The response (orange) of the full system, equation 2.1, during post-run-up for $I_{test} = -0.2$ pA starting from the equilibrium E_1 set by $I_{bias} = -2$ pA. The response is projected onto the two bifurcation diagrams of the membrane voltage V with respect to the inactivation variable h_A for $I_{app} = I_{bias}$ (faded colors) and $I_{app} = I_{test}$ (dark colors). The h_A -nullcline (magenta) is also plotted in the figure. (B) Magnification of the curves inside the blue box in panel A, highlighting dynamics near the left knees (SN₁) of the faded and dark bifurcation diagrams.

response of the system spends more time on the lower (stable) branch of the critical manifold of the fast subsystem inside the slow region.

Based on the discussion thus far, one might expect the latency to increase when I_{bias} decreases. However, that is not what we see; instead, we find that the first-spike latency significantly drops after the initial increase, generating a nonmonotonic profile. Figures 8A and 8B show a trajectory for the full system, equation 2.1, for $I_{bias} = -2$ pA superimposed on the bifurcation diagram of the fast subsystem, together with h_A -nullcline (the slowest variable) during post-run-up, as done in Figures 6 and 7. The equilibrium E_1 (which determines the initial condition of the trajectory) moves to much smaller values of V (about -70 mV). When the test current is set to $I_{test} = -0.2$ pA, the solution moves toward the lower stable branch of the critical manifold of the full system, equation 2.1, and tracks a short segment of it. The solution trajectory then leaves the branch of equilibria before reaching the slow region. This change in behavior of the response allows the trajectory to get around the slow region without passing through it. Nonetheless, the solution still travels a longer distance along the critical manifold compared to the two previous cases, slowing down propagation. However, the latency caused by traveling along this branch is significantly smaller relative to that induced by the slow region.

As indicated by Figure 4, the latency increases gradually while decreasing the holding potentials beyond the biphasic component of the profile.

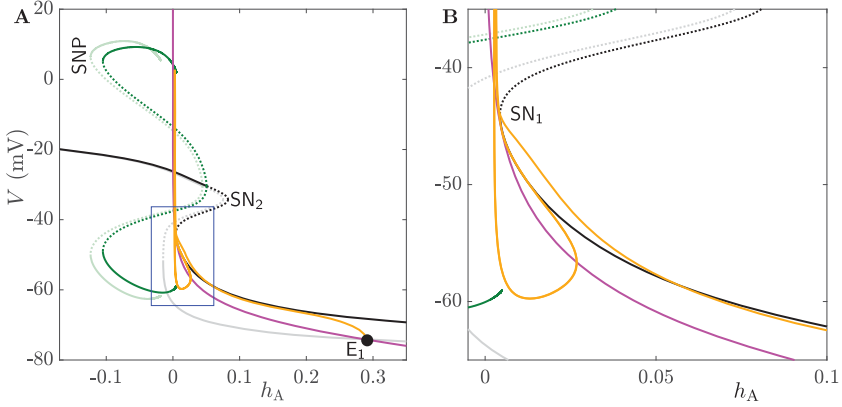


Figure 9: (A) The response (orange) of the full system, equation 2.1, during pre-run-up for $I_{\text{test}} = -0.15$ pA starting from the equilibrium E_1 set by $I_{\text{bias}} = -2$ pA. The response is projected onto the two bifurcation diagrams of the membrane voltage V with respect to the inactivation variable h_A for $I_{\text{app}} = I_{\text{bias}}$ (faded colors) and $I_{\text{app}} = I_{\text{test}}$ (dark colors). The h_A -nullcline (magenta) is also plotted in the figure. (B) Magnification of the curves inside the blue box in panel A, highlighting dynamics near the left knees (SN_1) of the faded and dark bifurcation diagrams.

Although the trajectory no longer passes through the slow region, traveling along the lower branch of stable equilibria of the fast subsystem (also associated with slow dynamics) is the reason for such an increase in first-spike latency. The hyperpolarization of V by applying a larger magnitude of I_{bias} keeps the solution longer along the branch of equilibria, which in turn makes the latency of the first spike longer. According to Figure 4, the latency during post-run-up (panel A) is higher than that associated with pre-run-up (panel B) for all holding potentials (V_{hold}). In other words, the latency profile in panel A is elevated compared to panel B, while the difference between the maximum and minimum latency is almost the same. To illustrate how the difference in latency between pre- and post-run-up is generated, we plot in Figure 9 the bifurcation diagrams of the fast subsystem during pre-run-up when $I_{\text{bias}} = -2$ pA (faded colors) and $I_{\text{test}} = -0.15$ pA (dark colors) and superimpose the h_A -nullcline (magenta) along with the solution trajectory induced by the step current (orange) on the diagram. Comparing the location of the stable equilibrium E_1 , formed by the h_A -nullcline and the critical manifold, in this figure to that seen during post-run-up in Figure 8, we see that E_1 is left-shifted in the former case (i.e., has lower h_A value), even though both are subjected to the same bias current $I_{\text{bias}} = -2$ pA. This allows the solution trajectory starting from E_1 to track the lower branch of the fast subsystem during pre-run-up for a longer distance, which increases

the latency to the first spike. For the results obtained here, we have chosen the difference between I_{test} and I_{SNIC} (i.e., $|I_{\text{test}} - I_{\text{SNIC}}|$) to be almost equal for both pre- and post-run-up to facilitate comparison.

3.3 Dual Role of Inhibition. Molineux et al. (2005) and, later, Mitry et al. (2020) suggested that increasing the magnitude of the presynaptic inhibitory input (g_{inh}) applied to the full system, equation 2.1, prior to an excitatory input with a fixed magnitude (g_{exc}) produces switching in responsiveness three times (Mitry et al., 2020). This suggests the presence of two regimes in the parameter space ($g_{\text{exc}}, g_{\text{inh}}$) in which the full system is either capable of generating an AP (responsive) or incapable of doing so (nonresponsive). In this section, we first show that switching in responsiveness during post-run-up depends only on g_{inh} , while during pre-run-up, it depends on g_{inh} and g_{exc} . We also explain how the existence of a connecting orbit determines the boundary between responsive and nonresponsive regimes in several parameter spaces defined by the four parameters: g_{inh} , g_{exc} , I_{bias} (the magnitude of the bias current applied immediately prior to presynaptic inhibition) and T_{inh} (the time duration of inhibition prior to the application of presynaptic excitation, referred to hereafter as “time to excitation”). We investigate this phenomenon during post-run-up and determine how all of these factors affect the switching phenomenon.

Figure 10A shows that the boundary between responsive and nonresponsive regimes in the three parameter spaces ($g_{\text{exc}}, g_{\text{inh}}$) A1, ($I_{\text{bias}}, g_{\text{inh}}$) A2, and ($T_{\text{inh}}, g_{\text{inh}}$) A3 is an S-shaped fold with two knees. In all of these panels, the nonresponsive (responsive) regime lies to the left (right) of the boundary. In Figure 10A1, the dashed line between the two knees of the S-shaped boundary shows that for a fixed magnitude of the excitatory input ($g_{\text{exc}} = 1.6$), the full system switches from responsive to nonresponsive and then back to responsive and finally switches to nonresponsive again while increasing g_{inh} . This is verified in Figure 10B, where four different values of g_{inh} along the dashed line in panel A1, labeled A^+ , B^- , C^+ , and D^- , are selected and time-series simulations of the full system, equation 2.1, are performed; at A^+ and C^+ (when $g_{\text{inh}} = 0, 2$ pS, respectively), the model is responsive, producing APs upon stimulation, while at B^- and D^- (when $g_{\text{inh}} = 1, 3$ pS, respectively), it is nonresponsive with no AP. The full system in all of these simulations is set at the equilibrium point E_1 with a holding potential of $V_{\text{hold}} = -54.57131$ mV, and each curve is divided into two segments, with the first (cyan) representing the response of the full system prior to excitation and the second (orange) representing the response after applying the excitatory input.

Similar outcomes to those obtained in Figure 10A1 are also observed for the two-parameter combinations ($I_{\text{bias}}, g_{\text{inh}}$) A2 and ($T_{\text{inh}}, g_{\text{inh}}$) A3 when considering the response of the full system to a pair of inhibitory/excitatory presynaptic inputs during post-run-up. In both cases, an S-shaped boundary between responsive (to the right of the boundary) and nonresponsive

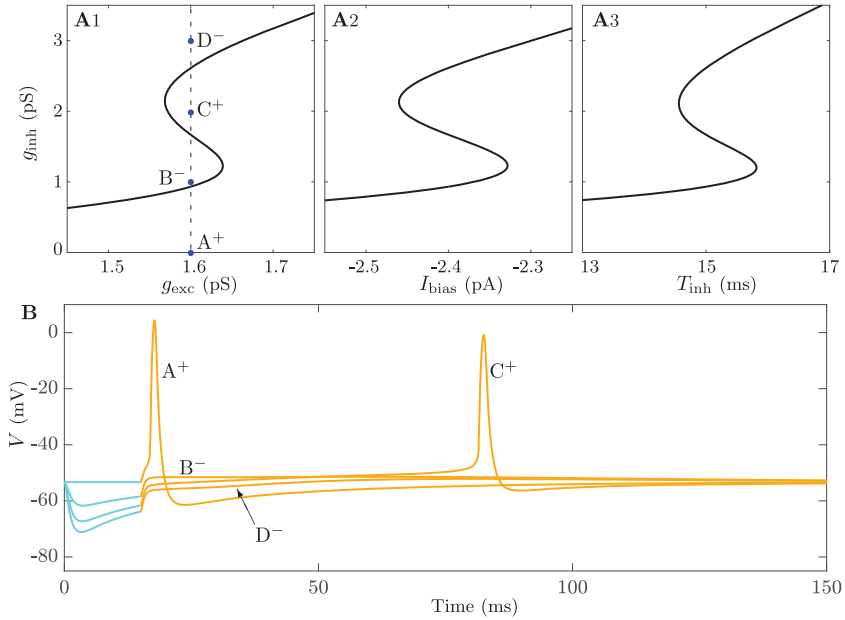


Figure 10: (A) The boundary between responsive and nonresponsive regimes of the full system, equation 2.1, during post-run-up in the $(g_{\text{exc}}, g_{\text{inh}})$ A1, $(I_{\text{bias}}, g_{\text{inh}})$ A2, and $(T_{\text{inh}}, g_{\text{inh}})$ A3 planes computed using the 2PBVP and continuation methods. The bias current is $I_{\text{bias}} = -0.24$ pA in panels A1 and A3. (B) Time-series simulations of the full system in response to a pair of inhibitory and excitatory presynaptic inputs separated by 15 ms as defined by equation 2.2. Each simulation includes two segments based on when the excitatory input is applied—cyan (orange): immediately prior to (after) excitatory input. The magnitudes of the inhibition and excitation used in panel B are indicated by the blue dots along the vertical dashed line in panel A1, denoted by A^+ , B^- , C^+ , and D^- . In these simulations, the holding potential is set at $V = -54.57131$ mV, when the model is unable to generate any spike.

(to the left of the boundary) regimes is obtained, allowing for switching between them when I_{bias} and T_{inh} , respectively, lie between the two knees of the boundary. The switching phenomenon in panel A1 has been studied in Mitry et al. (2020) where the authors manually computed the boundary by evaluating the response over an entire rectangular regime of interest in $(g_{\text{exc}}, g_{\text{inh}})$ -space. Here, the boundaries in Figure 10A are computed in a more systematic and efficient way using the 2PBVP and continuation methods described in section 2.4.

Based on the results obtained in Figure 10 for post-run-up, we can conclude that in the three parameter combinations considered here, the

magnitude of the inhibition (g_{inh}) is a key to producing switching (as suggested in Molineux et al., 2005). In particular, varying the magnitude of the excitation (g_{exc}) cannot lead to switching in responsiveness, implying that the profile of the excitatory input does not matter. This means that one can replace the latter by a square pulse of excitatory input, an important feature that will become clear later. Furthermore, based on the simulations performed in Figure 10B, the V -values of the C^+ curve prior to spiking (i.e., during the plateau phase) lie beneath the V -values of the B^- curve immediately following excitation (even though it does not exhibit an AP). That type of behavior was previously observed in experimental recordings (Molineux et al., 2005) and in model simulations (Mitry et al., 2020; Molineux et al., 2005). To understand the dynamics of this peculiar phenomenon, we need to use the reduced model, equation 2.3.

3.4 Presynaptic Input during Pre-Run-Up. Up to now, we have focused on the post-run-up behavior of the full system, equation 2.1. In this section, we use the pre-run-up parameter set (see Table 2) to study the switching phenomenon during pre-run-up and compare its underlying dynamics to that seen during post-run-up. We apply the same dynamic input, equation 2.2, used during post-run-up.

Figure 11 shows the boundary (solid line) between the responsive and nonresponsive regimes in the $(g_{\text{exc}}, g_{\text{inh}})$ -plane (panel A), together with six representative time-series simulations of the responses (panels B and C) at different parameter values within the $(g_{\text{exc}}, g_{\text{inh}})$ -plane (highlighted by the blue and red dots in panel A, respectively). In panel A, the g_{inh} -axis is shown in logarithmic scale for better visualization. The boundary in panel A is computed by continuing a response of equation 2.1 with a very large latency (see section 2.4 for more details). As shown, the boundary has two folded parts with four knees, allowing for switching in responsiveness to occur along the g_{inh} or g_{exc} directions when the other is kept fixed (compare to post-run-up in Figure 10A1). Switching between responsive and nonresponsive behaviors occurs along these folds. The time-series simulations of the full model during pre-run-up when g_{inh} (g_{exc}) are varied are shown in Figure 11B (Figure 11C) using the parameter combinations of $(g_{\text{exc}}, g_{\text{inh}})$ highlighted by the blue (red) dots. These parameters are labeled A^+ , B^- , and C^+ (α^+ , β^- and γ^+), on the vertical (horizontal) dashed line in Figure 11A. The blue (red) dots show that increasing the magnitude of the inhibition g_{inh} (excitation g_{exc}) while keeping the excitation g_{exc} (inhibition g_{inh}) fixed produces switching. More specifically, Figure 11B shows that for $g_{\text{exc}} = 3$ pS, the full system, equation 2.1, produces APs when $g_{\text{inh}} = 0$ (A^+), 3 pS (C^+) but does not do so when $g_{\text{inh}} = 1$ pS (B^-). Figure 11C shows that for $g_{\text{inh}} = 30$, the full system produces APs when $g_{\text{exc}} = 4.2$ (α^+), 5.7 pS (γ^+), but does not do so again when $g_{\text{exc}} = 5$ pS (β^-). In other words, unlike post-run-up, switching in responsiveness can occur in both directions: along increasing values of g_{inh} and g_{exc} while keeping the other fixed. Indeed, the full

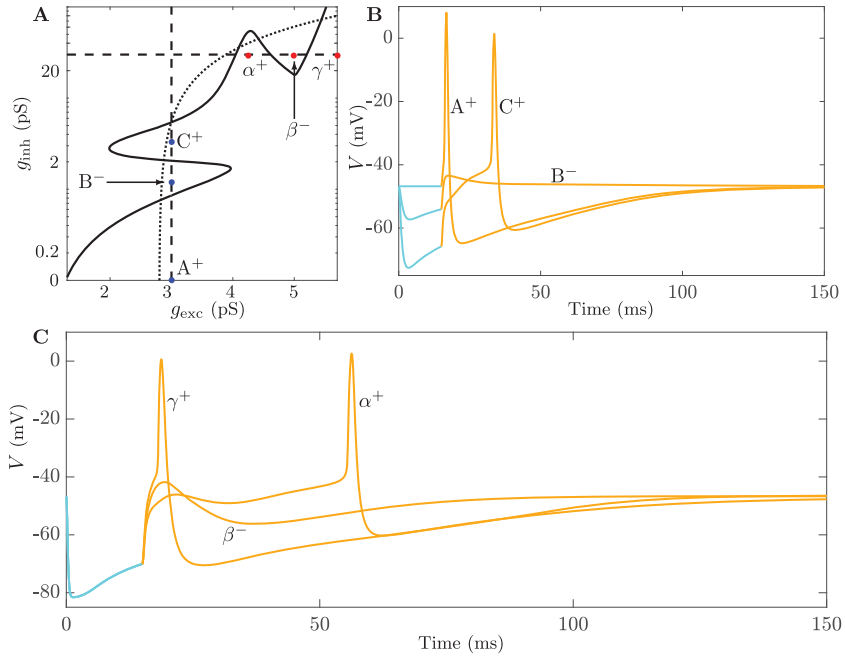


Figure 11: (A) The boundary between responsive and nonresponsive regimes of the full system, equation 2.1, during pre-run-up in the (g_{exc}, g_{inh}) -plane for $I_{bias} = -0.2$ pA computed using the 2PBVP and continuation methods. To improve visualization, g_{inh} is shown in logarithmic scale. The boundary exhibits two folds in the g_{exc} (upper fold) and g_{inh} (lower fold) directions, allowing for repetitive switching between responsiveness and nonresponsiveness to occur along the vertical dashed (when g_{exc} is fixed), horizontal dashed (when g_{inh} is fixed), and diagonal dotted lines. (B, C) Time-series simulations of the full system in response to a pair of inhibitory and excitatory presynaptic inputs as defined by equation 2.2. Each simulation includes two segments based on when the excitatory input is applied—cyan (orange): immediately prior to (after) excitatory input. The magnitudes of the inhibition and excitation used in panels B and C are indicated by the blue dots (labeled A^+ , B^- , C^+) and red dots (labeled α^+ , β^- , γ^+) along the vertical and horizontal dashed lines in panel A, respectively. In these simulations, the holding potential is set at $V = -46.80090$ mV, when the model is not able to generate any spike.

system can also produce switching seven times when the magnitudes of g_{inh} and g_{exc} are changed along the diagonal dotted line in Figure 11A. This suggests that the relative magnitudes of inhibition versus excitation play intricate roles in determining the response of stellate cells during pre-run-up (the more relevant model to the *in vivo* properties of stellate cells).

By targeting the conductances of some specific ion channels, one can control the size of the folded parts within the boundary during pre-run-up or even get rid of them altogether. The conductances of Na^+ and K^+ channels do not affect these folds (and thus the switching phenomenon), but the conductances of T-type Ca^{2+} or A-type K^+ channels do so. Specifically, decreasing g_T initially makes the knees of the lower fold closer while shifting the upper fold downward until it merges with the lower one, causing the repetitive switching phenomenon to disappear and the boundary to be without folds, that is, monotonic (results not shown). Similarly, increasing g_A makes the switching range with respect to g_{exc} smaller until it eventually disappears (results not shown).

In addition to the switching phenomenon, the full system, equation 2.1, during pre-run-up also exhibits this peculiar behavior associated with the firing threshold seen in Figure 10B during post-run-up in response to a pair of inhibitory/excitatory presynaptic inputs. Figures 10B and 11C show that the voltage amplitude in the time-series simulations for B^- and β^- , respectively, surpasses that of C^+ and γ^+ immediately prior to firing. We explain later the underlying dynamics governing this phenomenon for both post- and pre-run-up.

3.5 Dynamics of the Reduced Model. In this section, we show that although our model reduction approach causes changes in the behavior of the full system described by equation 2.1, the resulting reduced model described by equation 2.3 still preserves some of the dynamic properties of the full system during pre-run-up, including its responses to presynaptic inputs. Indeed, by plotting the bifurcation diagram of V of the reduced model with respect to I_{app} in Figure 12, we obtain a bifurcation structure similar to that seen in Figure 3. More specifically, we obtain a cubic-like critical manifold (black line), consisting of three branches of stable (solid) and unstable/saddle (dotted) equilibria that connect at saddle-node bifurcations (LP_1 for the lower two branches and LP_2 for the upper two branches), and envelopes of limit cycles (green lines), representing the maxima and minima of a family of stable (solid) and unstable (dotted) limit cycles. As in Figure 3, the bifurcation diagram in Figure 12 shows that an envelope of unstable limit cycles emanates from a subcritical Hopf bifurcation (H) in the upper branch of the critical manifold (where the equilibria switch their stability properties from stable to unstable) and meets an envelope of stable limit cycles at a saddle-node bifurcation of periodic orbits, denoted FP_1 . This later stable envelope undergoes two successive saddle-node bifurcations of periodic orbits, denoted FP_2 and FP_3 , and switches its stability properties at every point. Finally, the envelope of stable limit cycles that is formed after FP_3 terminates at a SNIC bifurcation that, as we have indicated, underlies type 1 excitability seen in the full model, equation 2.1.

To verify if the reduced model, equation 2.3, is able to generate the switching between responsive and nonresponsive regimes analogous to

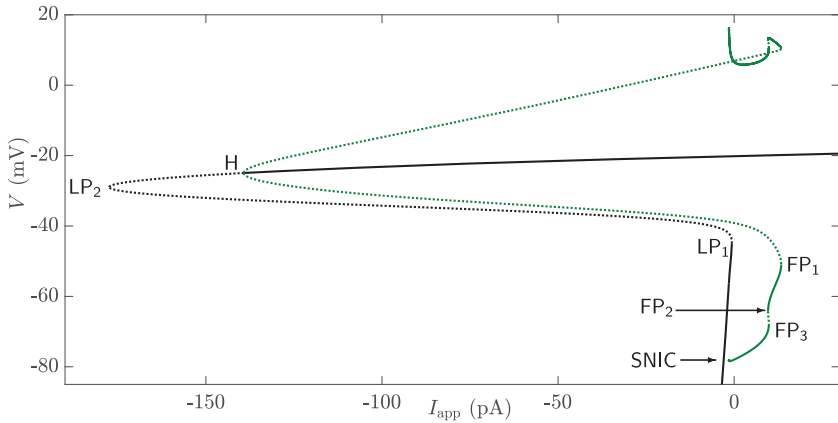


Figure 12: Bifurcation diagram of the reduced model, equation 2.3, with respect to I_{app} during pre-run-up. Black solid (dotted) lines indicate stable (unstable/saddle) branches of equilibria; green solid (dotted) lines show envelopes of stable (unstable) limit cycles. Two saddle-node bifurcations LP_1 and LP_2 connect three branches of equilibria of the reduced model. The envelope of unstable limit cycles emanating from a subcritical Hopf bifurcation (H) undergoes three successive saddle-node bifurcations of periodic orbits (FP_1 , FP_2 , and FP_3), switching stability at every bifurcation point. The envelope of stable limit cycle that eventually forms terminates at a SNIC bifurcation.

those seen in the full system, equation 2.1, we applied the modified presynaptic input defined by equation 2.4 to the reduced model. As indicated earlier, we use such a presynaptic input rather than the one defined by equation 2.2 because the application of a dynamic excitatory input will displace or deform the critical manifold of the system. Our results (not shown) reveal that for a fixed excitatory current pulse, the system switches three times between responsive and nonresponsive regimes when the magnitude of the inhibitory input is increased. These outcomes are identical to those obtained by the full system when subjected to such presynaptic input.

3.6 Stable Manifold of the Saddle Determines the Firing Threshold. Having shown that the reduced model captures some properties of the full system during pre-run-up, we aim next to use it to study how the firing threshold induced by presynaptic inputs is determined. With the performed modifications on the input protocol and reducing the pre-run-up full system, equation 2.1, to the pre-run-up reduced model, equation 2.3, we can compute the stable manifold of the saddle equilibrium associated with equation 2.3 and determine the relative position of the solution with respect to the manifold in defining the firing threshold. By explaining the switching phenomenon in this reduced model, we would be able to

deduce how switching is produced in the full system, equation 2.1, when the dynamic input, equation 2.2, is applied.

As indicated in Figure 12, when $I_{\text{app}} = -1.5$ pA, the reduced model, equation 2.3, has three equilibria: one stable on the lower branch, one saddle on the middle branch, and another stable on the upper branch, each denoted \mathcal{E}_1 , \mathcal{E}_2 , and \mathcal{E}_3 , respectively. The saddle equilibrium \mathcal{E}_2 has a one-dimensional unstable manifold and a two-dimensional stable manifold associated with one positive and two negative eigenvalues, respectively. We compute the stable manifold of \mathcal{E}_2 as a family of orbit segments using the 2PBVP and continuation methods in Auto (see section 2.4).

Figures 13A and 13B show a portion of the stable manifold $W^s(\mathcal{E}_2)$ (blue surface) of the saddle equilibrium \mathcal{E}_2 (red X) from two different angles plotted in the (h_T, n, V) -space. These panels also show a red dot that corresponds to the location of the stable equilibrium \mathcal{E}_1 for a given I_{bias} . Panels A and B show that close to the equilibrium \mathcal{E}_2 , the manifold looks like a horse saddle; it increases on the right and left sides and decreases from the other two sides at the back and front. The declining back side eventually plateaus, whereas for the rising sides, one of them plateaus on the left side and the other spirals and accumulates on itself on the right. In fact, the stable manifold accumulates on the stable manifold of a saddle periodic orbit in backward time that exists for this set of parameters and separates the attracting equilibria \mathcal{E}_1 from \mathcal{E}_3 . These spirals are small at one end and become larger at the other end, making the manifold extend to $+\infty$. When a presynaptic input is applied, this stable manifold may shift in the (h_T, n, V) -space. To resolve this problem, the presynaptic input defined by equation 2.4 is used; its excitation component is applied as a pulse (rather than as a dynamic input). Moreover, the dynamic inhibition is removed as soon as the excitation is applied. The absence of an excitatory input guarantees that the stable manifold of the saddle \mathcal{E}_2 remains frozen in time and fixed in space after removing excitation without affecting its switching properties.

To illustrate how the stable manifold of \mathcal{E}_2 determines how the response of the reduced model to a presynaptic input defined by equation 2.4, we superimpose in Figures 13C to 13E three solution trajectories generated by such a presynaptic input while varying the magnitude of the inhibition (g_{inh}). As indicated before, the reduced model, equation 2.3, can become nonresponsive for intermediate magnitudes of the inhibition (g_{inh}) while keeping the excitatory input fixed. In Figures 13C to 13E, we choose $g_{\text{inh}} = 0$ pS (responsive, panel C), 1 pS (nonresponsive, panel D), and 2.5 pS (responsive, panel E) and keep the excitatory pulse I_{exc} fixed at 4.1 pA for 5 ms. Each solution is divided into three orbit segments: the first segment (cyan) is formed during the application of the inhibitory input, the second segment (orange) is formed during the application of the excitatory input after removing the inhibition, and the last segment (green) is the remaining portion of the trajectory when the presynaptic input is removed completely.

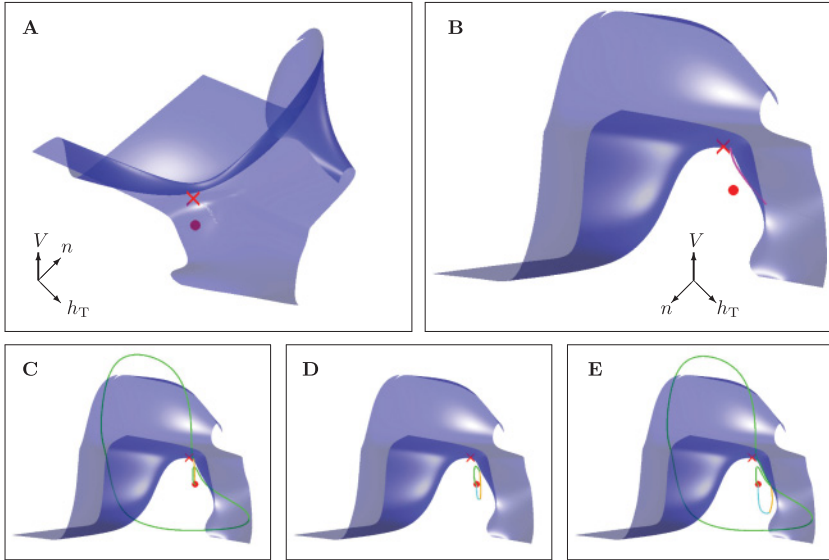


Figure 13: (A) Stable manifold $W^s(\mathcal{E}_2)$ (blue surface) of the saddle equilibrium \mathcal{E}_2 (red X) of the reduced model, equation 2.3, during pre-run-up. The red dot is the stable equilibrium \mathcal{E}_1 (functioning as the initial condition for one solution trajectory). (B) Another view of $W^s(\mathcal{E}_2)$, together with the response curve (magenta line) formed by the set of all points within a family of solution trajectories when the presynaptic inputs are removed. (C–E) Three representative solution trajectories of the reduced model induced by presynaptic inputs defined by, equation 2.4, starting from the stable equilibrium \mathcal{E}_1 . Trajectories are divided into three segments based on the presynaptic input; cyan (orange) segments correspond to the inhibitory (excitatory) portion of the presynaptic input immediately prior to (after) the excitatory (inhibitory) input, while the green segment corresponds to the remaining part of the trajectories when the presynaptic input is removed.

For $g_{\text{inh}} = 0$ and 2.5 pS, the reduced model, equation 2.3, generates a spike in the form of a trajectory in the (h_T, n, V) -space that starts from the stable equilibrium \mathcal{E}_1 , makes a large excursion around the manifold $W^s(\mathcal{E}_2)$, and returns to the same side as \mathcal{E}_2 (see Figures 13C and 13E). For $g_{\text{inh}} = 1$ pS, the reduced model does not generate a spike, and its solution quickly returns to the stable equilibrium \mathcal{E}_1 . The superposition of the responses generated by the reduced model onto the stable manifold of Figure 13A shows that the two-dimensional stable manifold $W^s(\mathcal{E}_2)$ of the saddle equilibrium \mathcal{E}_2 acts as a separatrix for each response. Removing the excitatory input while the trajectory is still below the manifold, where the stable equilibrium \mathcal{E}_1 lies, causes a quick return to \mathcal{E}_1 . However, when the input is removed and

the trajectory is on the other side of $W^s(\mathcal{E}_2)$, the reduced model generates a large excursion (i.e., an AP) around the manifold to reach \mathcal{E}_1 . The reason that the trajectory returns back to \mathcal{E}_1 rather than converging to \mathcal{E}_3 is because of the stable manifold of the saddle-type periodic orbit, defining the boundary of the basin of attraction of \mathcal{E}_3 . Although the stable manifold of \mathcal{E}_2 is displaced or deformed upon the removal of the excitatory input pulse, it remains fixed during the application of the excitatory pulse and after its removal.

The three responses shown in Figures 13C to 13E are representative of the switching phenomenon that occurs with the reduced model during an increase in g_{inh} . When considering a whole family of such trajectories over an entire range of $g_{\text{inh}} \in [0, 50]$ pS, one can generate a response curve (the magenta line in Figure 13B) formed by the set of all points where trajectories switch from orange (induced by excitation) to green (not induced by any presynaptic input). This response curve possesses three segments depending on its location relative to the stable manifold $W^s(\mathcal{E}_2)$. The first segment lies on top of $W^s(\mathcal{E}_2)$, which means that the response of the reduced model has to make a large excursion to reach the other side of the manifold before settling back at the stable equilibrium \mathcal{E}_1 . The second segment, in the middle of the response curve, lies underneath the manifold $W^s(\mathcal{E}_2)$, on the same side as \mathcal{E}_1 . This means that the reduced model, equation 2.3, generates only graded responses in which trajectories return to the equilibrium as soon as the excitation is removed. Finally, the third segment lies on top of $W^s(\mathcal{E}_2)$, producing outcomes similar to those seen with the first segment of the response curve. In other words, the response curve (magenta) intersects the stable manifold $W^s(\mathcal{E}_2)$ twice, allowing the reduced model to exhibit switching behavior at each crossing. Further analysis of the response curve shows that it actually intersects the manifold a third time in the back of the manifold for higher values of g_{inh} (not shown in Figure 13 to allow for visual clarity). This is to be expected in view of the fact that excitable systems do not fire when the magnitude of the inhibition is too high. Given that the three intersections between the response curve and the manifold $W^s(\mathcal{E}_2)$ lie on the manifold, it means that the response trajectories associated with these particular points eventually converge to the equilibrium \mathcal{E}_2 , creating a connecting orbit between the attracting equilibrium \mathcal{E}_1 and the saddle equilibrium \mathcal{E}_2 . Based on this, we can conclude that the boundary between the responsive and nonresponsive regimes is determined by the stable manifold of the saddle equilibrium $W^s(\mathcal{E}_2)$ (i.e., $W^s(\mathcal{E}_2)$ acts as a separatrix between the two regimes). Moreover, the first-spike latency of trajectories in the responsive regime increases when the excitation is removed at a point closer to $W^s(\mathcal{E}_2)$. Unlike the slow dynamics induced by the ghost of the SNIC in section 3.2, the increase in latency here is due to the slow flow close to the saddle equilibrium \mathcal{E}_2 . In fact, when the response lies close to $W^s(\mathcal{E}_2)$, it tracks the manifold toward \mathcal{E}_2 and spends a significant amount of time in its vicinity before returning to \mathcal{E}_1 .

The underlying dynamics of this switching phenomenon is identical to that seen in the post-run-up model, with the stable manifold of the saddle playing a key role in defining the threshold (results not shown). In other words, the saddle equilibrium preserves its effects in producing switching during run-up in cerebellar stellate cells.

3.7 Implications on the Full System. The analysis of the three-dimensional reduced model when subjected to a brief fixed excitation pulse can provide us with good insight into how the full system, equation 2.1, behaves with a dynamic presynaptic input. By using the original dynamic input protocol given by equation 2.2, which changes with time, the manifold $W^s(E_2)$ shifts slightly during excitation but eventually settles back to its original location as time goes to infinity, when excitatory presynaptic input exponentially converges to 0. Increasing the magnitude of the inhibitory input pushes the full system response trajectories toward the manifold. For a certain magnitude of the inhibitory input, the trajectory lands on the manifold and converges to the saddle equilibrium E_2 . This creates a connecting orbit between the attracting equilibrium E_1 and the saddle equilibrium E_2 in a manner similar to that produced by the reduced model, equation 2.3. In fact, this connecting orbit is associated with the “coincidence” of the response curve (similar to the magenta line seen in Figure 13B) with the five-dimensional stable manifold of the saddle equilibrium $W^s(E_2)$. When the response curve is above $W^s(E_2)$ for certain magnitudes of the inhibition/excitation, the full system is responsive (fires APs), and when it is below $W^s(E_2)$, it is not (does not fire APs). The shape of the boundary between the responsive and nonresponsive regimes of Figure 8A1 is thus dictated by the shape of the manifold and how it interacts with the (g_{exc}, g_{inh}) -plane.

Figure 14 shows two responses of the full system, equation 2.1, during pre-run-up superimposed onto the bifurcation diagram of the fast subsystem along with the h_A -nullcline (see also Figure 5). Two trajectories are plotted when $g_{exc} = 3$ pS and $g_{inh} = 0.85370$ pS (see panel A) or $g_{inh} = 2.05334$ pS (see panel B), respectively, and color-coded cyan and orange based on when the inhibition and excitation are applied as explained in Figures 13C to 13E. In both cases, the pair of (g_{exc}, g_{inh}) lies at the intersections of the S-shaped boundary and the dashed line in Figure 10 (i.e., they coincide with where the response curve intersects with the $W^s(E_2)$). As expected, the two trajectories formed by these two pairs eventually converge to the saddle equilibrium E_2 (see Figure 14).

4 Summary and Conclusion

In this study, we investigated the dynamic properties of a Hodgkin–Huxley type of model previously developed in Molineux et al. (2005) and later revised in Mitry et al. (2020). We demonstrated that the model, labeled the full system, produces several features associated with neuronal excitability

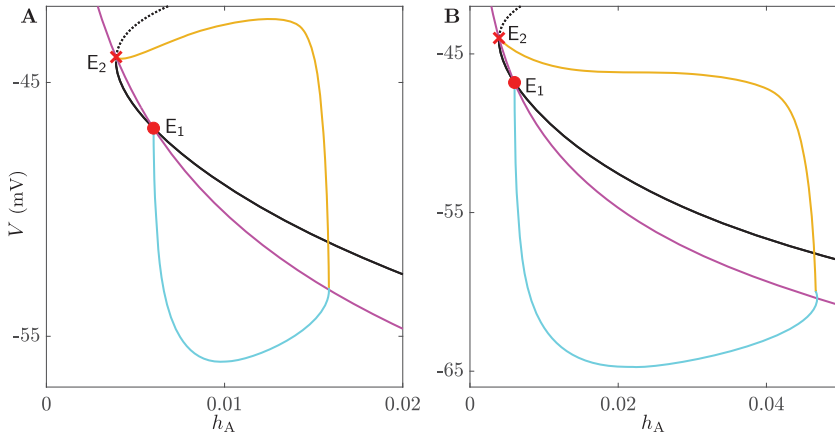


Figure 14: Responses of the full system, equation 2.1, to dynamic inputs with $g_{\text{exc}} = 0.3$ pS and (A) $g_{\text{inh}} = 0.85370$ pS, or (B) $g_{\text{inh}} = 2.05334$ pS superimposed onto the bifurcation diagram of the fast subsystem in Figure 5 during pre-run-up. The black line is the critical manifold of the fast subsystem, close to SN_1 , consisting of stable (solid) and unstable (dotted) branches; the magenta line is the h_A -nullcline; cyan/orange lines show the trajectories color-coded based on when the inhibition (cyan) and excitation (orange) are applied during a presynaptic input. Notice that for a certain combination of inhibition and excitation, the solution trajectories starting from the stable equilibrium E_1 (red dot) can eventually land on the saddle equilibrium E_2 (red X).

that are consistent with those observed in cerebellar stellate cells. More specifically, it produces the nonmonotonic first-spike latency during both pre- and post-run-up upon the application of a current-step protocol that consists of a bias current (I_{bias}), of varying amplitudes, and a fixed test current (I_{test}). It also produces the switching phenomenon, in which the full system alternates between two different states: responsive (able to generate an action potential, AP) and nonresponsive (unable to generate an AP), when the amplitude of an inhibitory presynaptic input, preceding an excitatory one, is increased. Using continuation techniques in the software package Auto, we developed a two-point boundary value problem (2PBVP) setup to recompute some of the results in Mitry et al. (2020) in a more systematic manner. The efficiency of these methods allowed us to investigate the potential role of other factors in the responsiveness of the system. By applying slow-fast analysis and the 2PBVP method, we were able to provide a detailed explanation as to how the nonmonotonic first-spike latency is generated, to compute the stable manifold of a saddle and thus illustrate its role in generating the switching phenomenon.

As Mitry et al. (2020) showed we verified that the full system is a type 1 oscillator possessing a saddle-node bifurcation on an invariant cycle (SNIC) when the membrane voltage is plotted as a function of I_{app} . Mitry et al. (2020) showed that the nonmonotonic latency during pre- and post-run-up is caused by the “ghost of the SNIC” that forms when a system’s dynamics is very close to (but not yet at) a saddle-node bifurcation. Using slow-fast analysis, we examined the effects of the SNIC bifurcation on first-spike latency of the full system. Exploiting this approach, we were able to show how the creation of a slow passage between the nullcline of the slow variable (h_A) and the critical manifold of the full system increases the latency significantly (creating a bottleneck effect). This increase is finite for values of $I_{\text{app}} = I_{\text{test}}$ larger than $I_{\text{app}} = I_{\text{SNIC}}$. The latency decreases significantly when the response of the full system does not pass through the ghost of the SNIC. Our results revealed that the effect of the initial condition on the latency is not as significant compared to that produced by the ghost of the SNIC; however, the initial condition does play a role when the solution of the full system induced by a step current is not affected by the ghost of the SNIC. In this case, we showed that the distance from the SNIC bifurcation or the attracting limit cycle (measured using the arc length) is not the main factor in explaining the gradual increase in the first-spike latency, but rather the traveling time of the solution when following the critical manifold. When the holding potential decreases, the A-type K^+ is activated, causing the response of the full system to track the critical manifold in the (h_A, V) -plane for a longer distance. The slow flow along this lower branch of the critical manifold as a result creates longer latencies. When plotting the h_A -nullcline on top of the critical manifold of the full system, we obtained three steady states—two stable equilibria and one of saddle type. We found that the invariant stable manifold of the saddle equilibrium divides the various trajectories emanating from different initial conditions (holding potentials) into two groups: ones that pass through the slow region associated with the ghost of the SNIC and others that do not. The latter group shows an increase in first-spike latency when moving along the critical manifold.

As suggested by Figure 1, the gating variable h_T is also slow, with a timescale comparable to that for h_A . One can thus analyze the dynamics of the full system, equation 2.1, using slow-fast analysis by assuming that it has two slow variables: h_A and h_T . Doing so produces three-dimensional bifurcation structures whose intersections with the (h_A, V) -plane are identical to those displayed in Figures 5 and 9 (results not shown). This indicates that extending our analysis to two slow variables would not provide additional information on how slow dynamics through the ghost of the SNIC and lower stable branch of the critical manifold are produced in the full system.

For the second feature, the switching phenomenon, we showed that it occurs while varying the magnitude of inhibition g_{inh} and keeping the magnitude of excitation g_{exc} fixed in a presynaptic input defined by

equation 2.2. This was consistent with previous experimental observations showing that g_{inh} is key to producing switching (Molineux et al., 2005). Using a 2PBVP and continuation methods, we calculated systematically the boundary between responsive and nonresponsive regions within the $(g_{\text{exc}}, g_{\text{inh}})$ -, $(g_{\text{inh}}, I_{\text{bias}})$ -, and $(g_{\text{inh}}, T_{\text{inh}})$ -planes and showed that all exhibit an S-shaped fold. Previously, this boundary was calculated during post-run-up by discretely scanning an entire domain of interest within the $(g_{\text{exc}}, g_{\text{inh}})$ -space.

Based on the shape of the boundaries, we concluded that the profile of excitatory input does not affect the switching phenomenon during post-run-up and that identical results can be obtained by replacing this component of the dynamic input (i.e., excitation) by a short current square pulse. To further study the underlying dynamics of this phenomenon, we formulated a three-dimensional reduced model, given by equation 2.3, from the full system, equation 2.1, generated by replacing the activation variable of A-type K^+ current (m_{A}) with the activation variable of the delayed rectifier K^+ current (n), the inactivation variable of Na^+ current by $1 - n$, and the inactivation variable of A-type K^+ current (h_{A}) by the inactivation variable of T-type Ca^{2+} current (h_{T}). Using the resulting three-dimensional reduced model, we were able to establish that the type 1 excitability and switching in responsiveness seen in the full system are preserved. We computed the two-dimensional stable manifold of the saddle equilibrium of the reduced model to speculate what underlies the switching phenomenon in the full system. Our results revealed that the position of this stable manifold relative to the solution trajectories upon the removal of presynaptic inputs of varying g_{inh} determines whether an AP can be generated. We argued that some solution trajectories starting from the stable equilibrium lying below the stable manifold of the saddle actually cross the manifold upon excitation, loop around it, and return back to the stable equilibrium forming an AP (responsive), while those that do not cross end up generating a graded response by returning to the stable equilibrium immediately (non-responsive). Crossing the stable manifold of the saddle is thus determined by where exactly solution trajectories lie relative to the manifold in state-space upon the application of the excitatory presynaptic input. By plotting the set of all such points in (h_{T}, n, V) -space (see the magenta line in Figure 13B), we obtained a response curve that intersects the stable manifold of the saddle equilibrium three times, giving rise to the switching phenomenon.

The reduced model, equation 2.3, along with the simplification applied on the excitatory component of the presynaptic input, helped us gain good insight into the dynamics of the full system injected with the original dynamic input, equation 2.4. We defined the boundary between responsive and nonresponsive regimes in the $(g_{\text{exc}}, g_{\text{inh}})$ -plane as a connection between a stable equilibrium and a saddle equilibrium and used it to compute the stable manifold of the saddle. The S-shaped fold of the boundary allows for switching to occur between responsive and nonresponsive regimes. We

found that the configuration of the stable manifold of the saddle equilibrium dictates the shape of that boundary and when a trajectory can fire an AP or not.

We also investigated the dynamics of the full system, equation 2.1, during pre-run-up characterized by having higher first-spike latencies compared to post-run-up. In the pre-run-up case, our calculations showed that the switching phenomenon occurs not only with respect to g_{inh} when g_{exc} is kept fixed but also with respect to g_{exc} while keeping g_{inh} fixed. This was due to the fact that the boundary between responsive and nonresponsive regimes exhibits two folds allowing switching to occur seven times along a diagonal line crossing the boundary six times (see Figure 11A). In general, we found this phenomenon to be more pronounced during pre-run-up compared to post-run-up, highlighting its importance to stellate cell excitability in vivo.

Changing the conductances of Na^+ and K^+ currents did not affect the folds of the boundary (switching phenomenon); however, increasing A-type K^+ conductance or decreasing the T-type Ca^{2+} conductance removed these folds altogether and made repetitive switching between the two regimes disappear. Detecting these outcomes experimentally is quite challenging in the pre-run-up case, as the cell may run up during electrophysiological recording in whole-cell configuration.

The inhibitory and excitatory inputs that stellate cells receive from different sources create very complicated dynamics in their response, which in turn affects the GABAergic presynaptic inputs onto Purkinje cells, the primary output of the cerebellum. Providing a deep understanding of the dynamic properties of stellate cells can thus shed light on the behavior of the entire network within the cerebellum in vivo.

Acknowledgments

This work was supported by a discovery grant from the Natural Sciences and Engineering Council of Canada to A.K. and an operating grant from the Canadian Institutes of Health Research (Funding reference number: 142431) to D.B. The work presented here benefited greatly from discussions with John Mitry.

References

- Albus, J. S. (1971). A theory of cerebellar function. *Mathematical Biosciences*, 10, 25–61.
- Alexander, R. P. D., Mitry, J., Sareen, V., Khadra, A., & Bowie, D. (2019). Cerebellar stellate cell excitability is coordinated by shifts in the gating behavior of voltage-gated Na^+ and a-type K^+ channels. *eNeuro*, 6(3), 1–17.
- Anderson, D., Mehaffey, W. H., Iftinca, M., Rehak, R., Engbers, J. D. T., Hameed, S., ... Turner, R. W. (2010). Regulation of neuronal activity by Cav3-Kv4 channel signaling complexes. *Nature Neuroscience*, 13(3), 333–337.

- Arshavsky, Y. I., & Orlovsky, G. N. (1986). *Role of the cerebellum in the control of rhythmic movements*. London: Palgrave Macmillan.
- Börgers, C. (2017). *An introduction to modeling neuronal dynamics*. Cham, Switzerland: Springer.
- Brooks, V. B., & Thach, W. T. (2011). *Cerebellar control of posture and movement*. New York: American Cancer Society.
- Desroches, M., Guckenheimer, J., Krauskopf, B., Kuehn, C., Osinga, H. M., & Wechselberger, M. (2012). Mixed-mode oscillations with multiple time scales. *SIAM Review*, 54(2), 211–288.
- Doedel, E. J. (1981). Auto: A program for the automatic bifurcation analysis of autonomous systems. *Congr. Numer.*, 30(3), 265–284.
- Doedel, E. J., & Oldeman, B. E. (2010). *AUTO-07p: Continuation and bifurcation software for ordinary differential equations*. Montreal: Department of Computer Science, Concordia University. <http://www.cmv1.cs.concordia.ca/>
- Eccles, J., Llinás, R., & Sasaki, K. (1964). Excitation of cerebellar Purkinje cells by the climbing fibres. *Nature*, 203(4942), 245–246.
- Ermentrout, B. G., & Terman, D. H. (2010). *Mathematical foundations of neuroscience*. New York: Springer.
- Farjami, S., Alexander, R. P. D., Bowie, D., & Khadra, A. (2019). Switching in cerebellar stellate cell excitability in response to a pair of inhibitory/excitatory pre-synaptic inputs: A dynamical system perspective. Anmar Khadra repository, http://www.medicine.mcgill.ca/physio/khadralab/code_NeuralComput1.html
- Farjami, S., Kirk, V., & Osinga, H. M. (2018). Computing the stable manifold of a saddle slow manifold. *SIAM Journal on Applied Dynamical Systems*, 17, 350–379.
- Fernandez, F. R., Engbers, J. D. T., & Turner, R. W. (2007). Firing dynamics of cerebellar Purkinje cells. *Journal of Neurophysiology*, 98(1), 278–294.
- Franci, A., Drion, G., & Sepulchre, R. (2012). An organizing center in a planar model of neuronal excitability. *SIAM Journal on Applied Dynamical Systems*, 11(4), 1698–1722.
- Häusser, M., & Clark, B. A. (1997). Tonic synaptic inhibition modulates neuronal output pattern and spatiotemporal synaptic integration. *Neuron*, 19, 665–678.
- Holmes, G. (2000). The cerebellum of man. *Brain*, 62, 1–30.
- Izhikevich, E. M. (2000). Neural excitability, spiking and bursting. *International Journal of Bifurcation and Chaos*, 10, 1171–1266.
- Izhikevich, E. M. (2006). *Dynamical systems in neuroscience: The geometry of excitability and bursting*. Cambridge, MA: MIT Press.
- Keener, J., & Sneyd, J. (2009). *Mathematical physiology I: Cellular physiology*. New York: Springer.
- Korn, H., & Axelrad, H. (1980). Electrical inhibition of Purkinje cells in the cerebellum of the rat. *Proceedings of the National Academy of Sciences of the United States of America*, 77(10), 6244–6247.
- Krauskopf, B., Osinga, H. M., Doedel, E. J., Henderson, M. E., Guckenheimer, J., Vladimirovsky, A., ... Junge, O. (2005). A survey of methods for computing (un)stable manifolds of vector fields. *International Journal of Bifurcation and Chaos*, 15, 763–791.

- Krauskopf, B., & Riess, T. (2008). A Lin's method approach to finding and continuing heteroclinic connections involving periodic orbits. *Nonlinearity*, *21*, 1655–1690.
- Krinskii, V. I., & Kokoz, Y. M. (1973). Analysis of the equations of excitable membranes I. Reduction of the Hodgkin-Huxley equations to a second order system. *Biofizika*, *18*(3), 506–511.
- Liu, S. J., Lachamp, P., Liu, Y., Savtchouk, I., & Sun, L. (2011). Long-term synaptic plasticity in cerebellar stellate cells. *Cerebellum*, *7*(4), 559–562.
- Llano, I., & Marty, A. (1995). Presynaptic metabotropic glutamatergic regulation of inhibitory synapses in rat cerebellar slices. *Journal of Physiology*, *486*, 163–176.
- Miall, C. R. (2013). *Cerebellum: Anatomy and function*. New York: Springer.
- Midtgaard, J. (1992a). Membrane properties and synaptic responses of Golgi cells and stellate cells in the turtle cerebellum in vitro. *Journal of Physiology*, *457*, 329–354.
- Midtgaard, J. (1992b). Stellate cell inhibition of Purkinje cells in the turtle cerebellum in vitro. *Journal of Physiology*, *457*, 355–367.
- Mitry, J., Alexander, R. P. D., Farjami, S., Bowie, D., & Khadra, A. (2020). Modeling excitability in cerebellar stellate cells: Temporal changes in threshold, latency and frequency of firing. *Communications in Nonlinear Science and Numerical Simulation*, *82*, 105014.
- Mittmann, W., Koch, U., & Häusser, M. (2005). Feed-forward inhibition shapes the spike output of cerebellar Purkinje cells. *Journal of Physiology*, *563*(2), 369–378.
- Molineux, M. L., Fernandez, F. R., Mehaffey, W. H., & Turner, R. W. (2005). A-type and *t*-type currents interact to produce a novel spike latency voltage relationship in cerebellar stellate cells. *Journal of Neuroscience*, *47*, 10863–10873.
- Morton, S. M., & Bastian, A. J. (2004). Cerebellar control of balance and locomotion. *Neuroscientist*, *10*(3), 247–259.
- Palay, S. L., & Chan-Palay, V. (1974). *Cerebellar cortex: Cytology and organization*. New York: Springer.
- Rinzel, J., & Baer, S. M. (1988). Threshold for repetitive activity for a slow stimulus ramp: A memory effect and its dependence on fluctuations. *Biophysical Journal*, *54*(3), 551–555.
- Sardanyés, J. (2009). Ghosts in high dimensional non-linear dynamical systems: The example of the hypercycle. *Chaos, Solitons and Fractals*, *39*(1), 92–100.
- Sherman, A. S., & Ha, J. (2017). How adaptation makes low firing rates robust. *Journal of Mathematical Neuroscience*, *7*(4), 1–21.
- Wolf, U., Rapoport, M. J., & Schweizer, T. A. (2009). Evaluating the affective component of the cerebellar cognitive affective syndrome. *Journal of Neuropsychiatry and Clinical Neurosciences*, *21*(3), 245–253.